Simulation of Heavily Irradiated Silicon Pixel Detectors

M. Swartz, D. Kim
Johns Hopkins University, Baltimore, MD 21218, USA
V. Chiochia, Y. Allkofer, C. Amsler, C. Regenfus, T. Speer
Physik Institut der Universität Zürich-Irchel, 8057 Zürich, Switzerland
A. Dorokhov, C. Hörmann, K. Prokofiev
Physik Institut der Universität Zürich-Irchel, 8057 Zürich, Switzerland and
Paul Scherrer Institut, 5232 Villigen PSI, Switzerland
D. Kotlinski, T. Rohe
Paul Scherrer Institut, 5232 Villigen PSI, Switzerland
D. Bortoletto, S. Son
Purdue University, West Lafayette, IN 47907, USA
S. Cucciarelli, M. Konecki
Institut für Physik der Universität Basel, 4056 Basel, Switzerland
L. Cremaldi, D. A. Sanders
University of Mississippi, University, MS 38677, USA

We show that doubly peaked electric fields are necessary to describe grazing-angle charge collection measurements of irradiated silicon pixel sensors. A model of irradiated silicon based upon two defect levels with opposite charge states and the trapping of charge carriers can be tuned to produce a good description of the measured charge collection profiles in the fluence range from 0.5×10^{14} $\mathrm{n_{eq}/cm^2}$ to 5.9×10^{14} $\mathrm{n_{eq}/cm^2}$. The model correctly predicts the variation in the profiles as the temperature is changed from $-10°\mathrm{C}$ to $-25°\mathrm{C}$. The measured charge collection profiles are inconsistent with the linearly-varying electric fields predicted by the usual description based upon a uniform effective doping density. This observation calls into question the practice of using effective doping densities to characterize irradiated silicon. The model is now being used to calibrate pixel hit reconstruction algorithms for CMS.

1. Introduction

A silicon pixel detector [1] is currently being developed for the CMS experiment at the CERN Large Hadron Collider (LHC). The detector will be a key component in the reconstruction of primary and secondary vertices in the particularly harsh LHC environment characterized by large track multiplicities and high radiation backgrounds. The innermost layer, located at only 4 cm from the beam line, is expected to be exposed to a 1 MeV neutron equivalent fluence of 3×10^{14} $\mathrm{n_{eq}/cm^2}$ per year at full luminosity.

The response of the silicon sensors during the detector operation is of great concern. It is well understood that the intra-diode electric fields in these detectors vary linearly in depth reaching a maximum value at the p-n junction. The linear behavior is a consequence of a uniform space charge density, N_{eff}, caused by thermally ionized impurities in the bulk material. It is well known that the detector characteristics are affected by radiation exposure, but it is generally assumed that the same picture is valid after irradiation. In fact, it is common to characterize the effects of irradiation in terms of a varying effective uniform charge density. In [2] we have proved that this picture does not provide a good description of irradiated silicon pixel sensors. In addition, it was shown that it is possible to adequately describe the charge collection characteristics of a heavily irradiated silicon detector in terms of a tuned double junction model which pro-

duces a doubly peaked electric field profile across the sensor. The modeling is supported by the evidence of doubly peaked electric fields obtained directly from beam test measurements and presented in [3]. The dependence of the modeled trap concentrations upon fluence was presented in [4] and the temperature dependence of the model was presented in [5]. We summarize these results in this document.

This paper is organized as follows: Section 2 describes the experimental details, Section 3 describes the carrier transport simulation used to interpret the data. The tuning of the double junction model and its resulting predictions are discussed in Section 4. The temperature dependence of the data and model are summarized in Section 5. The conclusions are given in Section 6.

2. Experimental Details

The measurements were performed in the H2 beam line of the CERN SPS in 2003/04 using 150-225 GeV pions. The beam test apparatus is described in [6]. A silicon beam telescope [7] consisted of four modules each containing two 300 μm thick single-sided silicon detectors with a strip pitch of 25 μm and readout pitch of 50 μm. The two detectors in each module were oriented to measure horizontal and vertical impact coordinates. A pixel hybrid detector was mounted between the second and third telescope modules on a

cooled rotating stage. A trigger signal was generated by a silicon PIN diode. The analog signals from all detectors were digitized in a VME-based readout system by two CAEN (V550) ADCs and one custom-built flash ADC. The entire assembly was located in an open-geometry 3T Helmholtz magnet that produced a magnetic field either parallel or orthogonal to the beam. The temperature of the tested sensors was controlled with a Peltier cooler that was capable of operating down to -30°C. The telescope information was used to reconstruct the trajectories of individual beam particles and to achieve a precise determination of the particle hit position in the pixel detector. The resulting intrinsic resolution of the beam telescope was about 1 μm.

The prototype pixel sensors are so-called "n-in-n" devices: they are designed to collect charge from n^+ structures implanted into n–bulk silicon using p-spray isolation. All test devices were 22×32 arrays of 125×125 μm^2 pixels that were fabricated by CiS. The substrate, produced by Wacker, was 285 μm thick, n-doped, diffusively-oxygenated float zone silicon of orientation $\langle 111 \rangle$, resistivity 3.7 kΩ·cm and oxygen concentration in the order of 10^{17} cm^{-3}. Individual sensors were diced from fully processed wafers after the deposition of under-bump metalization and indium bumps. A number of sensors were irradiated at the CERN PS with 24 GeV protons. The irradiation was performed without cooling or bias. The delivered proton fluences scaled to 1 MeV neutrons by the hardness factor 0.62 [8] were 0.5×10^{14} n$_{eq}$/cm^2, 2×10^{14} n$_{eq}$/cm^2 and 5.9×10^{14} n$_{eq}$/cm^2. All samples were annealed for three days at 30°C. In order to avoid reverse annealing, the sensors were stored at -20°C after irradiation and kept at room temperature only for transport and bump bonding. All sensors were bump bonded to PSI30/AC30 readout chips [9] which allow analog readout of all 704 pixel cells without zero suppression. The PSI30 settings were adjusted to provide a linear response to input signals ranging from zero to more than 30,000 electrons.

3. Sensor simulation

The interpretation of the test beam data relies upon a detailed sensor simulation that includes the modeling of irradiation effects in silicon. The simulation, PIXELAV [2, 10, 11], incorporates the following elements: an accurate model of charge deposition by primary hadronic tracks (in particular to model delta rays); a realistic 3-D intra-pixel electric field map; an established model of charge drift physics including mobilities, Hall Effect, and 3-D diffusion; a simulation of charge trapping and the signal induced from trapped charge; and a simulation of electronic noise, response, and threshold effects. The intra-pixel electric field map was generated using TCAD 9.0 [12] to

simultaneously solve Poisson's Equation, the carrier continuity equations, and various charge transport models. A final simulation step reformatted the simulated data into test beam format so that it could be processed by the test beam analysis software.

The simulation was checked by comparing simulated data with measured data from an unirradiated sensor. A plot of the charge measured in a single pixel as a function of the horizontal and vertical track impact position for normally incident tracks is shown in Fig. 1. The simulation is shown as the solid histogram and the test beam data are shown as solid points. Note that the sensor simulation does not include the "punch-through" structure on the n^+ implants which is used to provide a high resistance connection to ground and to provide the possibility of on-wafer IV measurements. There is reduced charge collection from this portion of the implant and the data shows reduced signal in both projections at the bias dot. Another check, shown in Table I, is the comparison of the average Lorentz angle measured at several bias voltages [6]. In both cases, reasonable agreement is observed between measured and simulated data.
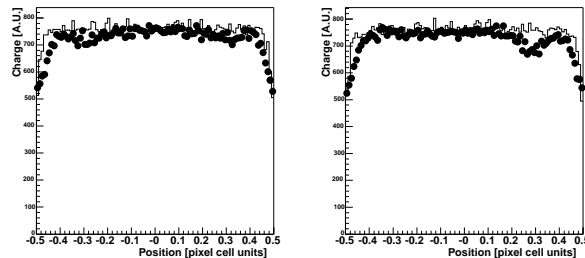

Figure 1: Collected charge measured in a single pixel as a function of the horizontal (left) and vertical (right) track impact position for tracks that are normally incident on an unirradiated sensor. The simulation is shown as a solid histogram and the test beam data are shown as solid dots.

Table I Measured and simulated values of average Lorentz angle θ_L versus bias voltage for an unirradiated sensor.

Bias Voltage	Measured θ_L [deg]	Simulated θ_L [deg]
150V	22.8 ± 0.7	24.7 ± 0.9
300V	14.7 ± 0.5	17.4 ± 0.9
450V	11.2 ± 0.5	12.0 ± 0.9

The effect of irradiation was implemented in the TCAD simulation by including two defect levels in the forbidden silicon bandgap with opposite charge states and trapping of charge carriers. The model, similar to

one proposed in [13], is based on the Shockley-Read-Hall (SRH) statistics and produces an effective space charge density ρ_{eff} from the trapping of free carriers in the leakage current. The effective charge density is related to the occupancies and densities of traps as follows,

$$\rho_{\text{eff}} = e\left[N_D f_D - N_A f_A\right] + \rho_{\text{dopants}} \qquad (1)$$

where: N_D and N_A are the densities of donor and acceptor trapping states, respectively; f_D and f_A are the occupied fractions of the donor and acceptor states, respectively, and ρ_{dopants} is the charge density due to ionized dopants (describes the resistivity of the material before irradiation). The donor and acceptor occupancies are related to the trap parameters by standard SRH expressions

$$f_D = \frac{v_h \sigma_h^D p + v_e \sigma_e^D n_i e^{E_D/kT}}{v_e \sigma_e^D (n + n_i e^{E_D/kT}) + v_h \sigma_h^D (p + n_i e^{-E_D/kT})} \qquad (2)$$

$$f_A = \frac{v_e \sigma_e^A n + v_h \sigma_h^A n_i e^{-E_A/kT}}{v_e \sigma_e^A (n + n_i e^{E_A/kT}) + v_h \sigma_h^A (p + n_i e^{-E_A/kT})}$$

where: v_e and v_h are the thermal speeds of electrons and holes, respectively; σ_e^D, σ_h^D are the electron and hole capture cross sections for the donor trap; σ_e^A, σ_h^A are the electron and hole capture cross sections for the acceptor trap; n, p are the densities of free electrons and holes, respectively; n_i is the intrinsic density of carriers; E_D, E_A are the activation energies (relative to the mid-gap energy) of the donor and acceptor states, respectively. Note that the single donor and acceptor states model the effects of many physical donor and acceptor states making the two-trap model an "effective theory".

The physics of the model is illustrated in Fig. 2. The space charge density and electric field are plotted as functions of depth z for a model tuned to reproduce the $\Phi = 5.9 \times 10^{14} \text{n}_{\text{eq}} \text{cm}^{-2}$ charge collection data at 150V bias. The SRH process produces electron-hole pairs more or less uniformly across the thickness of the sensor. As the electrons drift to the n+ implant, the total electron current increases as z decreases. The hole current similarly increases with increasing z. Trapping of the mobile carriers produces a net positive space charge density near the p+ backplane and a net negative space charge density near the n+ implant. Since positive space charge density corresponds to n-type doping and negative space charge corresponds to p-type doping, there are p-n junctions at both sides of the detector. The electric field in the sensor follows from a simultaneous solution of Poisson's equation and the continuity equations. The resulting z-component of the electric field varies with an approximately quadratic dependence upon z having a minimum at the zero of the space charge density and maxima at both implants. A more detailed descrip-

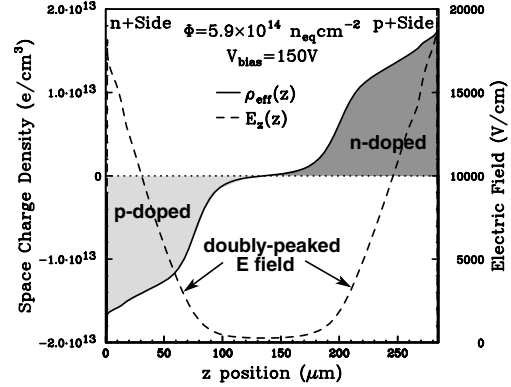tion of the double junction model and its implementation can be found in [2].

Figure 2: The space charge density (solid line) and electric field (dashed line) at $T = -10°C$ as functions of depth in a two-trap double junction model tuned to reproduce the $\Phi = 5.9 \times 10^{14} \text{n}_{\text{eq}} \text{cm}^{-2}$ charge collection data at 150V bias.

4. Model tuning and results

Charge collection across the sensor bulk was measured using the "grazing angle technique" [14]. As is shown in Fig. 3, the surface of the test sensor is oriented by a small angle (15°) with respect to the pion beam. Several samples of data were collected with zero magnetic field and at temperature of $-10°C$ and $-25°C$. The charge measured by each pixel along the y direction samples a different depth z in the sensor. Precise entry point information from the beam telescope is used to produce finely binned charge collection profiles.
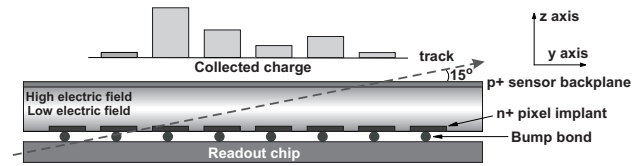

Figure 3: The grazing angle technique for determining charge collection profiles. The charge measured by each pixel along the y direction samples a different depth z in the sensor.

The charge collection profiles for a sensor irradiated to a fluence of $\Phi = 5.9 \times 10^{14}$ $\text{n}_{\text{eq}}/\text{cm}^2$ and operated at a temperature of $-10°C$ and bias voltages of 150V and 300V are presented in Fig 4. The measured profiles are shown as solid dots and the simulated profiles are shown as histograms. In order to investigate the applicability of the traditional picture of type-inverted silicon after irradiation, the simulated

profiles were generated with electric field maps corresponding to two different effective densities of acceptor impurities. The full histograms are the simulated profile for $N_{\text{eff}} = 4.5 \times 10^{12}$ cm^{-3}. Note that the 300V simulation reasonably agrees with the measured profile but the 150V simulation is far too broad. The dashed histograms show the result of increasing N_{eff} to 24×10^{12} cm^{-3}. At this effective doping density, the width of the simulated peak in the 150V distribution is close to correct but it does not reproduce the "tail" observed in the data at large y. The 300V simulated distribution is far too narrow and the predicted charge is lower than the data (note that the profiles are absolutely normalized). It is clear that a simulation based upon the standard picture of a constant density of ionized acceptor impurities cannot reproduce the measured profiles.
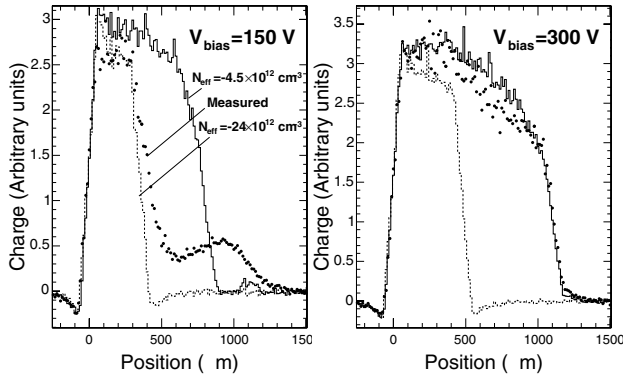

Figure 4: The measured and simulated charge collection profiles for a sensor at $T = -10°$C irradiated to a fluence of $\Phi = 5.9 \times 10^{14}$ n$_{\text{eq}}$/cm^2. The profiles measured at bias voltages of 150V and 300V are shown as solid dots. The full histograms are the simulated profiles for a constant effective doping $N_{\text{eff}} = 4.5 \times 10^{12}$ cm^{-3} of acceptor impurities. The dashed histograms are the simulated profiles for a constant effective doping $N_{\text{eff}} = 24 \times 10^{12}$ cm^{-3}.

The same measured profiles and those from bias voltages of 200V and 450V are shown in Fig. 5. They are compared with simulations based upon the electric field produced by the two trap model. The model has six free parameters (N_D, N_A, σ_e^D, σ_h^D, σ_e^A, σ_h^A) that can be adjusted. The activation energies are kept fixed to the values of [13]: $E_D = E_V + 0.48$ eV, $E_A = E_C - 0.525$ eV where E_V and E_C are the energies of the valence and conduction band edges. The electric field map produced by each TCAD run is input into PIXELAV. The electron and hole trapping rates, Γ_e and Γ_h, are also inputs to PIXELAV and are treated as constrained parameters. Although they have been measured [15], they are uncertain at the 20% level due to the fluence uncertainty and possible annealing of the sensors. They are therefore allowed to vary by as much as ±20% from their nom-

inal values. The donor concentration of the starting material is set to 1.2×10^{12} cm^{-3} corresponding to a full depletion voltage of about 70 V for an unirradiated device. Because each model iteration took approximately two days, it was not possible to use standard statistical fitting techniques. The parameters of the double junction model were systematically varied and the agreement between measured and simulated charge collection profiles was judged subjectively. The "best fits" shown in this paper are probably not true likelihood minima and the calculation of eight parameter error matrices is beyond available computational resources. Adequate agreement was achieved by setting the ratio of the common hole and electron cross sections σ_h/σ_e to 0.25 and the ratio of the acceptor and donor densities N_A/N_D to 0.40. There is a range of parameters in the N_D-σ_e space that produces reasonable agreement with the measured profiles. The range is shown in Fig. 6a as the solid line in the logarithmic space. If the donor density becomes too small ($N_D < 20 \times 10^{14}$ cm^{-3}), the 150V simulation produces too much signal at large z. If the donor density becomes too large ($N_D > 50 \times 10^{17}$ cm^{-3}), the 300V simulation produces insufficient signal at large z. Since the simulated leakage current varies as $I_{\text{leak}} \propto \sigma_e N_D$, different points on the allowed solid contour correspond to different leakage current. Contours of constant leakage current are shown as dashed curves and are labeled in terms of the corresponding damage parameter α where $\alpha_0 = 4 \times 10^{-17}$ A/cm is the expected leakage current [16]. It is clear that the simulation can accommodate the expected leakage current which is smaller than the measured current by a factor of three.

The electron and hole traps in the model should also contribute to the trapping of signal carriers. The contributions of these states to the effective trapping rates of electrons and holes are given by the following expressions

$$\Gamma_e = v_e \left[\sigma_e^A N_A (1 - f_A) + \sigma_e^D N_D f_D \right] \simeq v_e \sigma_e^A N_A$$
$$(3)$$
$$\Gamma_h = v_h \left[\sigma_h^D N_D (1 - f_D) + \sigma_h^A N_A f_A \right] \simeq v_h \sigma_h^D N_D$$

where it has been assumed that the trap occupancies are small. Because N_A/N_D is assumed to be constant, contours of constant electron trapping rate are parallel to contours of constant leakage current in N_D-σ_e space. The best "fit" of the simulation to the measured profiles reduced Γ_e to 85% of the un-annealed trapping rate Γ_0 for the nominal fluence [15]. These contours are compared with the allowed contour in Fig. 6b. It is clear that the simulation can accommodate the measured trapping rate in the same region of parameter space that maximizes the leakage current.

Figure 6b also suggests a solution to the puzzle that the trapping rates have been shown to be unaffected by the presence of oxygen in the detector bulk [15]
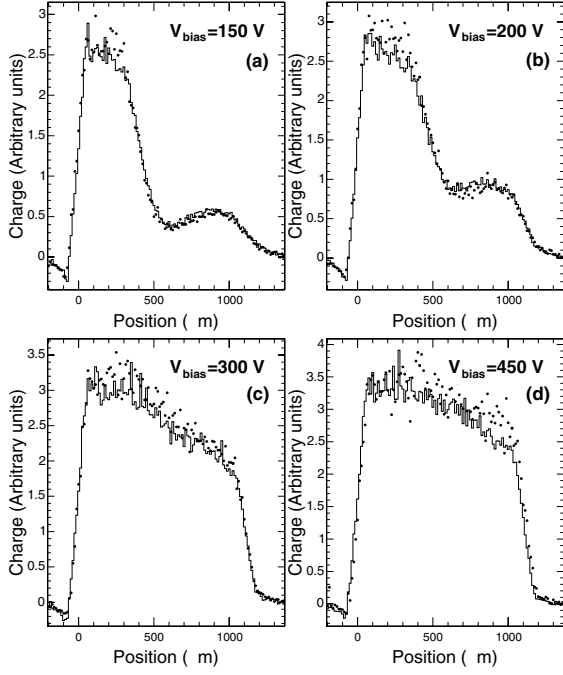
Figure 5: The measured charge collection profiles at a temperature of $-10°C$ and bias voltages of 150V, 200V, 300V, and 450V are shown as solid dots for a fluence of 5.9×10^{14} n_{eq}/cm^2. The two-trap double junction simulation is shown as the solid histogram in each plot.

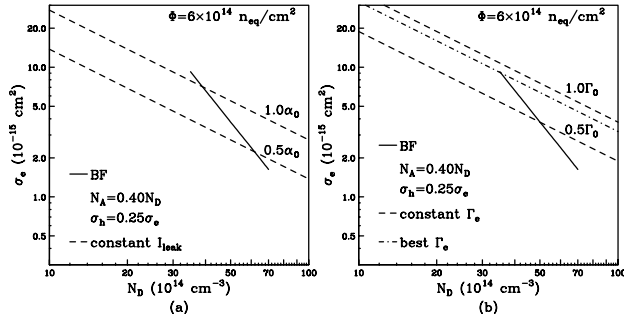Figure 6: The allowed region in the N_D-σ_e space for the best fit 5.9×10^{14} n_{eq}/cm^2 model is shown as the solid line in (a) and (b). Contours of constant leakage current are shown as dashed curves in (a) and are labeled in terms of the corresponding damage parameter α where $\alpha_0 = 4 \times 10^{-17}$ A/cm is the expected leakage current [16]. Contours of constant electron trapping rate are shown as dashed curves in (b) and are labeled in terms of the standard-annealed trapping rate Γ_0 for the nominal fluence [15].

whereas it is well-established that the space charge effects are quite sensitive to the presence of oxygen in the material [17]. It is clear from Fig 6b that small-cross-section trapping states can play a large role in the effective charge density but a small one in the effective trapping rates: every point on the dj44 line

produces 100% of the effective charge density but only the larger cross section points contribute substantially to the trapping rate. If the formation of the additional small-cross-section states were suppressed by oxygen, then ρ_{eff} could be sensitive to oxygenation whereas $\Gamma_{e/h}$ would be insensitive to oxygenation. This is another consequence of the observation that the occupancies $f_{D/A}$ of the trapping states are independent of the scale of the cross sections in the steady state (see eq. 3). The trapping of signal carriers is not a steady-state phenomenon and is sensitive to the scale of the trapping cross sections.

The simulation describes the measured charge collection profiles well both in shape and normalization. The "wiggle" observed at low bias voltages is a signature of the doubly peaked electric field shown in Fig. 2. The relative signal minimum near $y = 700$ μm (see Fig. 5) corresponds to the minimum of the electric field z-component, E_z, where both electrons and holes travel only short distances before trapping. This small separation induces only a small signal on the n^+ side of the detector. At larger values of y, E_z increases causing the electrons drift back into the minimum where they are likely to be trapped. However, the holes drift into the higher field region near the p^+ implant and are more likely to be collected. The net induced signal on the n^+ side of the detector therefore increases and creates the local maximum seen near $y = 900$ μm.

The charge collection profiles at $T = -10°C$ for sensors irradiated to fluences of $\Phi = 0.5 \times 10^{14}$ n_{eq}/cm^2 and $\Phi = 2 \times 10^{14}$ n_{eq}/cm^2 and operated at several bias voltages are presented in Fig. 7(a-c) and Fig. 7(d-g), respectively. The measured profiles, shown as solid dots, are compared to the simulated profiles, shown as histograms. Note that the "wiggle" is present at low bias even at $\Phi = 0.5 \times 10^{14}$ n_{eq}/cm^2 which is just above the "type-inversion" fluence. This suggests that a doubly peaked field is present even at rather small fluences.

The double junction model can provide a reasonable description of the lower fluence charge collection profiles using the parameters obtained with the fitting procedure shown in Table II. We observe that the donor trap concentration increases more rapidly with fluence than does the acceptor trap concentration. The ratio between acceptor and donor trap concentrations is 0.76 at the lowest fluence and decreases to 0.40 at 5.9×10^{14} n_{eq}/cm^2. In addition, the fits exclude a linear dependence of the trap concentrations with the irradiation fluence. At $\Phi = 5.9 \times 10^{14}$ n_{eq}/cm^2 the cross section ratio σ_h/σ_e is set to 0.25 for both donor and acceptor traps while at lower fluences we find $\sigma_h^A/\sigma_e^A = 0.25$ and $\sigma_h^D/\sigma_e^D = 1$ for the acceptor and donor traps, respectively. The simulated leakage current is approximately linear in fluence, but the ratio N_A/N_D is clearly not constant. This may be a consequence of the quadratic fluence scaling of one or more di-vacancy states or it may reflect the fact
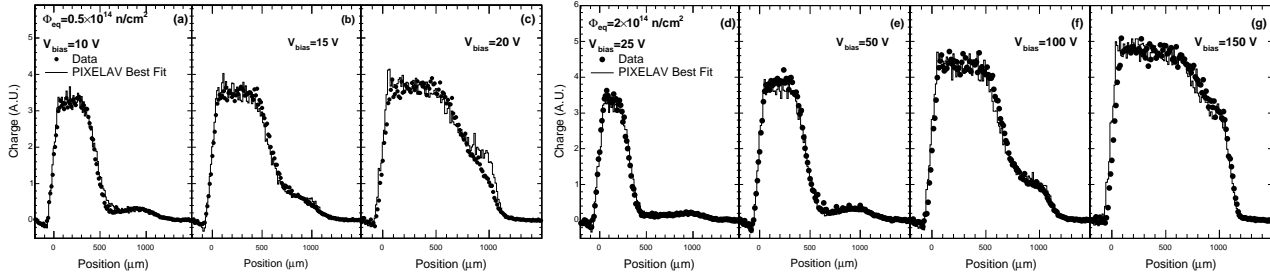
Figure 7: Measured (full dots) and simulated (histogram) charge collection profiles for sensors irradiated to fluences of 0.5×10^{14} n_{eq}/cm^2 (a-c) and 2×10^{14} n_{eq}/cm^2 (d-g), at $T = -10°C$ and several bias voltages.
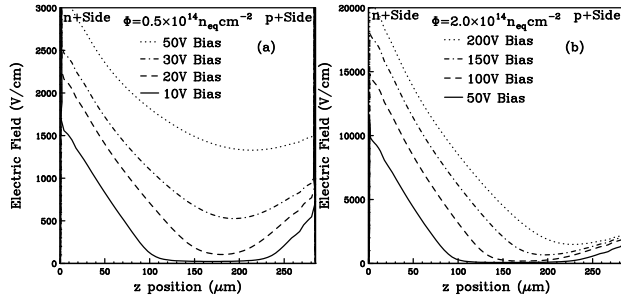

Figure 8: The z-component of the simulated electric field at $T = -10°C$ resulting from the model best fit is shown as a function of z for a sensor irradiated to fluences of 0.5×10^{14} n_{eq}/cm^2 (a) and 2×10^{14} n_{eq}/cm^2 (b).

that the two trap model with the particular choice of activation energies does not accurately model the dependence of the trap occupancies on leakage current. The allowed N_D-σ_e parameter spaces for the lower fluence models are much more constrained than in the Φ=5.9×10^{14} n_{eq}/cm^2 case and predict the expected leakage current. The electron and hole trapping rates, Γ_e and Γ_h are found to scale more or less linearly with fluence.

Table II Double trap model parameters extracted from the fit to the data.

Φ [10^{14} $n_{eq}cm^{-2}$]	0.5	2.0	5.9
N_A [10^{14} cm^{-3}]	1.9	6.8	16
N_D [10^{14} cm^{-3}]	2.5	10	40
$\sigma_e^{A/D}$ [10^{-15} cm^2]	6.60	6.60	6.60
σ_h^{A} [10^{-15} cm^2]	1.65	1.65	1.65
σ_h^{D} [10^{-15} cm^2]	6.60	6.60	1.65
Γ_e [10^{-2} ns^{-2}]	2.7	9.6	28.
Γ_h [10^{-2} ns^{-2}]	3.6	13.	38.

The z-component of the simulated electric field, E_z, is plotted as a function of z in Fig. 2 for $\Phi = 5.9 \times 10^{14}$ n_{eq}/cm^2 and in Fig. 8 for $\Phi = 0.5 \times 10^{14}$ n_{eq}/cm^2

and $\Phi = 2 \times 10^{14}$ n_{eq}/cm^2. At $\Phi = 5.9 \times 10^{14}$ n_{eq}/cm^2, the field profile has a minimum near the midplane of the detector which shifts toward the p+ implant at lower fluences. The field has maxima at the detector implants as discussed in Section 3. Figure 8(a) shows that a doubly peaked electric field is necessary to describe the measured charge collection profiles even at the lowest measured fluence which is just beyond the "type inversion point". The dependence of the space charge density upon the z coordinate is shown in Figures 2 and 9. Before irradiation the sensor is characterized by a constant and positive space charge density of 1.2×10^{12} cm^{-3} across the sensor bulk. After a fluence of 0.5×10^{14} n_{eq}/cm^2 the device shows a negative space charge density of about -1×10^{12} cm^{-3} for about 70% of its thickness, a compensated region corresponding to the E_z minimum and a positive space charge density close to the backplane. The space charge density and electric field near the p+ implant increase with fluence. The space charge density is not linear in z due to the variation of the carrier drift velocities with the electric fields.
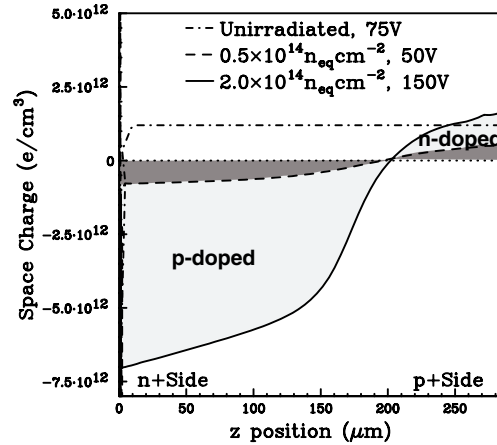

Figure 9: The simulated space charge density at $T = -10°C$ as a function of the z coordinate for fluences of 0.5×10^{14} n_{eq}/cm^2 and 2×10^{14} n_{eq}/cm^2.

5. Temperature dependence

The temperature dependence of the charge collection profiles was studied by accumulating data at $T = -25°C$. The PIXELAV simulation includes temperature dependent mobilities, diffusion, and trapping rates. The TCAD calculation of the electric field map is also based upon temperature dependent quantities including the bandgap energy and SRH lifetimes. The $T = -25°C$ charge collection profiles for the $\Phi = 2.0 \times 10^{14}$ n_{eq}/cm^2 and $\Phi = 5.9 \times 10^{14}$ n_{eq}/cm^2 sensors are compared with the simulation in Fig. 10. It is clear that the simulation correctly tracks the temperature-dependent variations in the measured profiles.
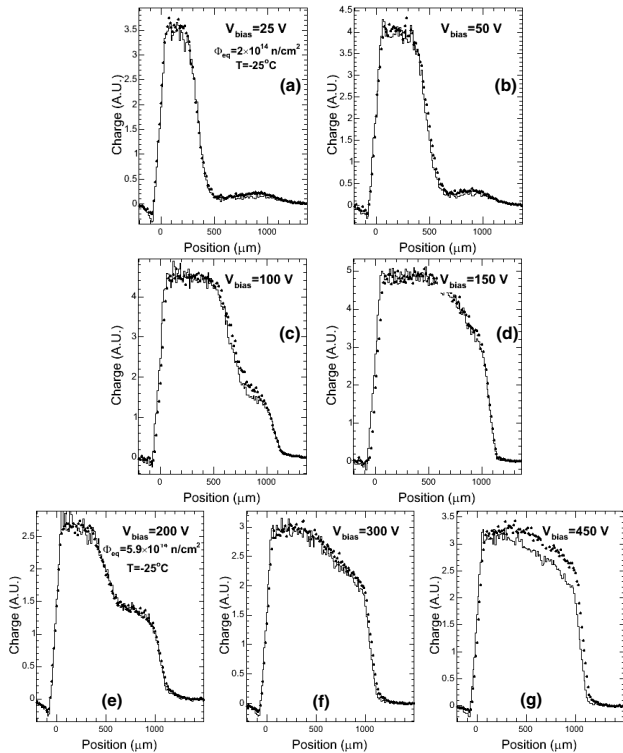

Figure 11: The simulated z-component of the electric field as a function of the z coordinate at the 5.9×10^{14} n_{eq}/cm^2 fluence for temperatures $T = -10°C$ and $T = -25°C$. The field profiles are shown for bias voltages of 150V and 300V.

Figure 10: Measured (full dots) and simulated (histogram) charge collection profiles at $T = -25°C$ and several bias voltages for sensors irradiated to fluences of 2.0×10^{14} n_{eq}/cm^2 (a-d) and of 5.9×10^{14} n_{eq}/cm^2 (e-g).

The effect of temperature on the z-component of the simulated electric field at $\Phi = 5.9 \times 10^{14}$ n_{eq}/cm^2 is shown in Fig. 11 for bias voltages of 150V and 300V. It is clear that decreasing the temperature also decreases the fields on the p+ side of the sensor and increases them on the n+ side.

6. Conclusions

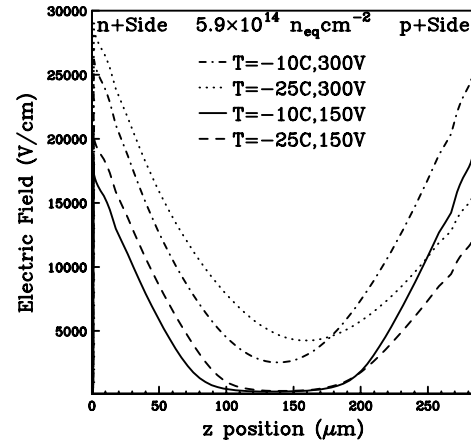In this paper we have shown that doubly peaked electric fields are necessary to describe grazing-angle charge collection measurements of irradiated silicon pixel sensors. A model of irradiated silicon based upon two defect levels with opposite charge states and the trapping of charge carriers can be tuned to produce a good description of the measured charge collection profiles in the fluence range from 0.5×10^{14} n_{eq}/cm^2 to 5.9×10^{14} n_{eq}/cm^2. The model correctly predicts the variation in the profiles as the temperature is changed from $-10°C$ to $-25°C$.

The doubly peaked electric field profiles have maxima near the implants and minima near the detector midplane. This corresponds to negative space charge density near the n^+ implant and and positive space charge density near the p^+ backplane. We find that it is necessary to decrease the ratio of acceptor concentration to donor concentration as the fluence increases. This causes the electric field profile to become more symmetric as the fluence increases. The effect of decreasing the temperature has the opposite effect of suppressing the fields on the p+ side of the sensor and increasing them on the n+ side.

The measured charge collection profiles of irradiated sensors are inconsistent with the linearly-varying electric fields predicted by the usual description based upon a uniform effective doping density. This suggests that the correctness and the physical significance of effective doping densities determined from capacitance-voltage measurements are quite unclear. In addition, we remark that the notion of partly depleted silicon sensors after irradiation is inconsistent with the measured charge collection profiles and with the observed doubly peaked electric fields.

The charge-sharing behavior and resolution functions of many detectors are sensitive to the details of the internal electric field. A known response func-

tion is a key element of an optimal reconstruction procedure. The effective model described in this paper is being used to calculate detailed response functions that are being incorporated into a new hit reconstruction algorithm for the CMS pixel tracking system [18, 19]. This will permit the "calibration" of the reconstruction algorithm to be tracked as the pixels are irradiated during LHC operation.

Acknowledgments

References

[1] CMS: The Tracker Project, Technical Design Report, CERN/LHCC 98-6. CERN, Switzerland.

[2] V. Chiochia, et al., IEEE Trans. Nucl. Sci. 52-4 (2005) 1067-1075, e-print: arXiv:physics/0411143.

[3] A. Dorokhov, et al., Nucl. Instrum. Meth. A560 (2006) 112–117, e-print: arXiv:physics/0412036.

[4] V. Chiochia *et al.*, to be published, Nucl. Instrum. Meth. A, e-print: arXiv:physics/0506228.

[5] M. Swartz *et al.*, to be published, Nucl. Instrum. Meth. A, e-print: arXiv:physics/0510040.

[6] A. Dorokhov, et al., Nucl. Instrum. Meth. A530 (2004) 71–76.

[7] C. Amsler, et al., Nucl. Instrum. Meth. A480 (2002) 501–507.

[8] M. Moll, E. Fretwurst, M. Kuhnke, and G. Linström, Nucl. Instrum. Meth. B186 (2001) 100-110.

[9] D. Meer, Bau und messen eines multichip pixelmodules als prototyp für den CMS-Tracker. Diplomarbeit, Eidgenössische Technische Hochschule, Zürich, Switzerland.

[10] M. Swartz, Nucl. Instrum. Meth. A511 (2003) 88–91.

[11] M. Swartz, CMS Note 2002/027, July 2002. http://cmsdoc.cern.ch/documents/02/note02_027.pdf

[12] TCAD 9.0 User's Manual, Synopsys, Inc., Mountain View CA. USA, http://www.synopsys.com.

[13] V. Eremin, E. Verbitskaya, Z. Li, Nucl. Instrum. Meth. A476 (2002) 556–564.

[14] B. Henrich, et al., CMS Note 1997/021, March 1997. http://cmsdoc.cern.ch/documents/97/note97_021.pdf

[15] G. Kramberger, V. Cindro, I. Mandić, M. Mikuž, and M. Zavrtanik, Nucl. Instrum. Meth., A481 (2002) 297.

[16] M. Moll, E. Fretwurst, and G. Lindström, Nucl. Instrum. Meth., A426 (1999) 87.

[17] G. Lindström, "Radiation damage in silicon detectors", Nucl. Instr. Meth. A512 (2003) 30-43. S. Dittongo, L. Bosisio, M. Ciacchi, D. Contarato, G. D'Auria, et al., "Radiation hardness of different silicon materials after high-energy electron irradiation", Nucl. Instr. Meth. A530 (2004) 110-116.

[18] V. Chiochia, E. Alagoz and M. Swartz, to be published, Nucl. Instrum. Meth. A, e-print: arXiv:physics/0512027.

[19] V. Chiochia, E. Alagoz and M. Swartz, to be published, Nucl. Instrum. Meth. A, e-print: arXiv:physics/0603192.